Advances in Ultrafast Gas-Phase X-ray Scattering

Advances in Ultrafast Gas-Phase X-ray Scattering

Advances in Ultrafast Gas-Phase X-ray Scattering

Brian Stankus[1], Haiwang Yong[2], Jennifer Ruddock[2,5], Lingyu Ma[2], Andres Moreno Carrascosa[2], Nathan Goff[2,4], Sébastien Boutet[4], Xuan Xu[2], Nikola Zotev[3], Adam Kirrander[3], Michael P. Minitti[4], Peter M. Weber[2,*]

[1] Department of Chemistry, Western Connecticut State University, Danbury, CT 06810, USA
[2] Department of Chemistry, Brown University, Providence, RI 02912, USA
[3] EaStCHEM, School of Chemistry, University of Edinburgh, David Brewster Road, Edinburgh EH9 3FJ, UK
[4] Linac Coherent Light Source, SLAC National Accelerator Laboratory, Menlo Park, CA, USA
[5] Present address: UES Inc., 4401 Dayton Xenia Rd., Dayton OH 45432
* Correspondence to: peter_weber@brown.edu

Abstract

Recent developments of x-ray free electron lasers and pulsed electron sources have enabled ultrafast scattering to become an increasingly powerful tool for exploring molecular dynamics. This article describes our recent experimental and methodological advances in ultrafast gas-phase x-ray scattering experiments at the LCLS. A re-designed short-pathlength windowless diffractometer is coupled with careful optimization of sample density and independent normalization of x-ray intensity fluctuations to provide gas-phase scattering patterns with exceptionally high signal-to-noise ratios. These advances, coupled with careful geometry optimization and data treatment, provide both ground- and excited-state signals in excellent agreement with high level *ab-initio* total scattering patterns.

1. Introduction

Chemistry, at its core, is the study of how atoms and molecules interact with each other to break and form chemical bonds to create new substances. Since its inception, chemists have explored these transformations by examining the products formed in molecular reaction mixtures. By varying reaction mixtures and characterizing the products, these experiments built an incredibly deep foundation of chemical intuition, based on which synthetic chemists have been able to create countless substances that transformed the world.

With the development of pump-probe experimental methodology and ultrafast laser systems, it has become possible to follow chemical reactions *in real time*.[1] This new branch of ultrafast chemistry includes a wide range of spectroscopic experiments that aim to measure the time evolution of reacting molecules. Just as these ultrafast spectroscopic measurements have generated a wealth of insight into real-time chemical reaction dynamics, it is expected that ultrafast scattering experiments can deepen our understanding of fundamental chemical processes.

While spectroscopy provides vital information about electronic and vibrational states and their time-evolution, it does not provide a direct probe of the molecular structure. In contrast, scattering measurements provide direct access to all interatomic distances in the molecule. The development of ultrashort-pulse electron sources and x-ray free electron lasers (XFELs) have allowed the implementation of electron and x-ray scattering experiments in the ultrafast domain[2,3]. Scattering techniques have been used to image electrocyclic reactions[4,5,6], measure coherent vibrational motions[7,8,9,10,11], monitor photodissociation reactions[2,12], determine the nature of electronically excited states[13,14,15], and measure the dynamics of various other

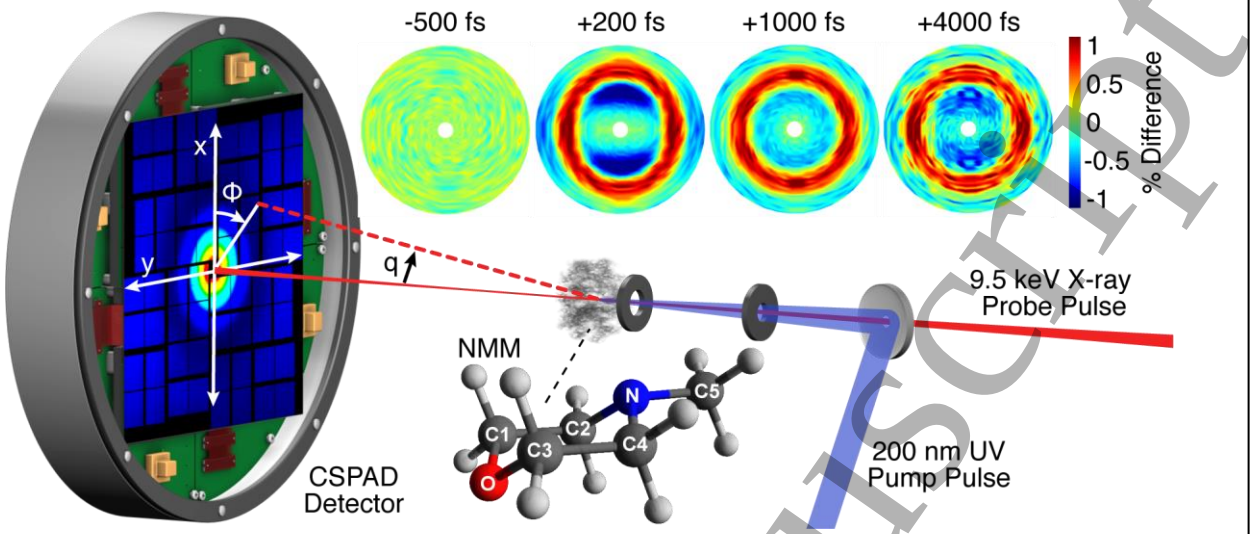

Figure 1. A schematic of the experimental setup. The target molecule (pictured here as N-methylmorpholine, NMM) is excited with a UV pump pulse, and the time-evolving molecular structure is probed via scattering with a hard x-ray probe pulse with a variable time delay. The percentage change in the scattering signal is shown as a function of the momentum transfer vector (q) and the azimuthal angle (ϕ) for several representative time delays in the top right. Figure reprinted from reference 7.

molecular systems[16,17]. These experiments provide information about the molecular structure of reacting molecules and constitute an important complement to spectroscopic measurements[18].

This article details this group's recent developments in the implementation and analysis of ultrafast gas-phase x-ray scattering experiments at LCLS. In this technique, a UV pump pulse is focused onto the gaseous target to initiate the photochemistry, and an x-ray probe pulse produces a scattering image at a variable time delay to monitor the dynamics (see Figure 1). Although the experiments are conceptually simple, successful implementation requires a wide array of considerations affecting the observed signal. Many features of the design for our initial study of the ring-opening of 1,3-cyclohexadiene[5] were described in a methods paper in 2016[19]. Since then, a number of advances have been made, both in the implementation and analysis of the experiment. This has led to improved signal-to-noise ratios, and has enabled more direct interpretation of observed scattering intensities.

It is often most convenient to express the measured time-resolved scattering signals as a percent difference (P_{diff}) relative to the unexcited molecular scattering signal:[4,20]

$$P_{diff}(\phi, q, t) = 100 \cdot \frac{I_{on}(\phi, q, t) - I_{off}(\phi, q)}{I_{off}(\phi, q)} \quad (1)$$

where $I_{on}(\phi, q, t)$ represents the scattering pattern measured at a given delay time t, and $I_{off}(\phi, q)$ represents the scattering pattern of the ground state, unreacted molecule. Expressing the measured signals in terms of percent difference, in addition to accentuating the relatively small changes in the scattering pattern over time, also completely cancels out any experimental artifacts common to both the UV-on and UV-off signals. This representation of the data eliminates a variety of factors, as described in Section 2.4.

Elements of x-ray scattering

The following provides a brief sketch of X-ray scattering, a topic covered in greater detail elsewhere[21,22,23]. It is worth noting that special considerations of the scattering theory must be taken in the context of x-ray scattering with pulses sufficiently short to resolve electron dynamics, which is not the case in the experiments discussed here[24,25,26,27]. Classic X-ray scattering by a free charged particle can be described by the Thomson scattering cross-section, which is the elastic scattering of electromagnetic radiation. For unpolarized primary X-ray beams, the intensity of elastic scattering by a single free electron is[28]:

$$I_{scatt}(2\theta) = \left(\frac{d\sigma_{Th}}{d\Omega}\right) \cdot \frac{I_0}{R^2} \cdot \left(\frac{1 + cos^2(2\theta)}{2}\right) \tag{2}$$

where I_0 and I_{scatt} are the incoming and scattered intensities ($\frac{W}{cm^2}$), R is the distance to the detector and $\frac{d\sigma_{Th}}{d\Omega} = \frac{e^4}{m_e{}^2 c^4} = 7.94 \times 10^{-26} cm^2$ is the differential Thomson cross section for a free electron. The scattering angle 2θ is related to the magnitude of the momentum transfer vector by $q = |\boldsymbol{k} - \boldsymbol{k_0}| = 2k_0 sin\theta$, where $\boldsymbol{k_0}$ is the incident wave vector $|\boldsymbol{k_0}| = \frac{2\pi}{\lambda}$ and $\boldsymbol{k}$ is the scattered wave vector.

The intensity can be connected to the number of photons per pulse by $I_0 = P_0 \frac{h \cdot \nu \cdot R_r}{A_0}$ and $I_{scatt} = P_{scatt} \frac{h \cdot \nu \cdot R_r}{A}$, where P_0 is the incoming photon count of the x-ray pulse, P_{scatt} is the number of scattered photons, R_r is the repetition rate of the XFEL, $h \cdot \nu$ is the photon energy, and A_0 and A are the areas of the incoming beam and the unit area on the detector. The probability of photons scattered into a resolution element Δq of the momentum transfer vector q can be expressed as[29]:

$$\frac{P_{scatt}(q, q + \Delta q)}{P_0} = \frac{d\sigma_{Th}}{d\Omega} \cdot \frac{1}{A_0 \cdot 2k_0^2} \cdot \left(1 + cos^2\left(2arcsin\frac{q}{2k_0}\right)\right) \cdot 2\pi q \cdot \Delta q \tag{3}$$

It is apparent that the scattering signal scales as the area of the resolution element $2\pi q \cdot \Delta q$ and the $cos^2(2\theta)$ dependence on the scattering angle.

When X-rays scatter from atoms or molecules, the elastic scattering form-factor is the Fourier transform of the atomic or molecular one-electron density $\rho(\boldsymbol{r})$, which can be obtained from electronic structure calculations. The elastic atomic form factor then reads:

$$f(q) = \int \rho(\boldsymbol{r}) e^{i\boldsymbol{q}\cdot\boldsymbol{r}} d\boldsymbol{r} \tag{4}$$

In order to calculate the form factor of molecules, it is common to invoke the independent atom model (IAM) approximation. The IAM treats the molecular electron density as a sum of spherical atomic densities, each centered at the position of the nuclei. Thus, within the IAM, the molecular form factor is given by:

$$f_{IAM}(q) = \sum_{\alpha=1}^{N_{at}} f_\alpha(q) e^{i\boldsymbol{r_\alpha}\cdot\boldsymbol{q}} \tag{5}$$

where $f_\alpha(q)$ are the atomic form factors, N_{at} is the number of atoms, and $\boldsymbol{r_\alpha}$ is the position of atom α. There are convenient tabulations for x-ray form factors for all atomic elements[30,31]. The scattering amplitude is modulated by the square of the form factor and averaging over the

random orientations of gas-phase molecules yields Debye's formula[32], which expresses the molecular intensity $I_M(q)$ of the isotropic total X-ray scattering signal as:

$$I_M(q) = \sum_{a=1}^{N_{at}}(|f_\alpha(q)|^2 + S_\alpha) + \sum_{\alpha\neq\beta}^{N_{at}} f_\alpha(q) f_\beta(q) \frac{\sin(q r_{\alpha\beta})}{q r_{\alpha\beta}} \quad (6)$$

where $r_{\alpha\beta} = |\boldsymbol{r_\alpha} - \boldsymbol{r_\beta}|$ is the interatomic distance and S_α is the net inelastic scattering term caused by Compton scattering, which can be conveniently obtained from the tabulated incoherent scattering functions of the elements[33,34].

The observed scattering signals depend on the scattering cross sections, the composition and structure of the investigated molecule, and the range of scattering angles subtended by the detector. The ratio of scattered to incoming photon numbers per pulse, from N molecules into a range of scattering vectors between q_1 and q_2 is[29]:

$$\frac{P_{scatt}(q_1,q_2)}{P_0} = \frac{d\sigma_{Th}}{d\Omega} \cdot \frac{\pi N}{A_0 k_0^2} \int_{q_1}^{q_2} I_M(q) \cdot \left(1 + cos^2\left(2arcsin\frac{q}{2k_0}\right)\right) \cdot q \cdot dq \quad (7)$$

As the number of molecules can be estimated for the given experimental conditions and the geometry of the sample cell, the approximate absolute number of scattered photons can be calculated using Equation (7).

While IAM often proves a useful first approximation for predicting overall scattering intensities, it is not able to correctly describe the distortions produced in the electron density as a consequence of the chemical bonding or to account for electronic excitations. An alternative way to obtain the x-ray scattering intensity and improve the modeling of molecular electronic structure is the formulation of total x-ray scattering intensity in terms of the *ab-initio* 2-electron reduced density matrix $\Gamma_{\alpha,\alpha(r_1,r_2)}$:

$$I_{tot}^{ai}(q) = \langle \int\int \Gamma_{\alpha,\alpha(r_1,r_2)} e^{iq(r_1-r_2)}\, dr_1\, dr_2 \rangle_{\theta,\phi} \quad (8)$$

Where $\langle ... \rangle_{\theta,\phi}$ represents the rotational averaging over all possible molecular orientations in the ensemble and α is the electronic state under study. $I_{tot}^{ai}(q)$, analogous to $I_M(q)$ in Equation 6, adequately describes the elastic and inelastic effects in the x-ray scattering process and not only improves the IAM approach but also accounts for the Compton effects, S_α, in a reliable way. The elastic component of the scattering signal, if required, can be derived from the previous equation by only considering the one-electron contributions via the electron density matrix $\rho(r)$:

$$I_{el}^{ai}(q) = \langle \int \rho(r) e^{iqr} dr \rangle_{\theta,\phi} \quad (9)$$

The calculation of the total and elastic x-ray scattering intensities can be carried out by using *ab-initio* calculated wavefunctions as outlined in references 44 and 35. It should be noted that the net inelastic scattering included in Eq. (6) corresponds to an approximation of the difference between the total scattering in Eq. (8) and the elastic scattering in Eq. (9). Notably, this component is not strictly independent of geometry or electronic state as implied by the IAM formula in Eq. (6)[35,44]. The *ab-initio* wavefunction-based method can be significantly more accurate than the IAM, especially for excited states, and both approaches will be used in the following depending on the accuracy required. We also note that the inelastic component is

important for gas-phase scattering since the relative enhancement of the elastic component that occurs in crystalline samples is absent.

2. Methods

The measurement of ultrafast gas-phase pump-probe x-ray scattering signals entails a variety of experimental challenges. Low sample density coupled with relatively low x-ray scattering cross-sections (compared to electron scattering) limits the intensity of the overall signal, which also decays rapidly with q. In addition, there are challenges associated with trying to measure changes in the scattering signal arising from a relatively small population of reacting molecules. Although it seems tempting to try to achieve a large population of excited molecules, the probability of optical excitation must be kept sufficiently low throughout the interaction region to minimize multi-photon absorption.

Beyond these fundamental challenges, there are also a variety of obstacles to the practical implementation of the experimental design. In addition to proper calibration of time delay and x-ray intensity, one must also consider the difficulty of spatially and temporally overlapping the optical and x-ray beams in the interaction region that is housed inside a vacuum chamber. Clearly, successful implementation of such experiments requires careful consideration of a variety of intricate design details, many of which are discussed below.

2.1 Diffractometer design

The scattering cell features a windowless design so as to avoid scattering of the intense primary x-ray beam by any window material. At the entrance side, the openings are made of platinum apertures, which block stray radiation and define the x-ray beam position. At the exit side, a hole in the beryllium window transmits the primary x-ray beam. The scattered x-rays traverse the beryllium, but their intensity is so low that further scattering by the window material can be neglected.

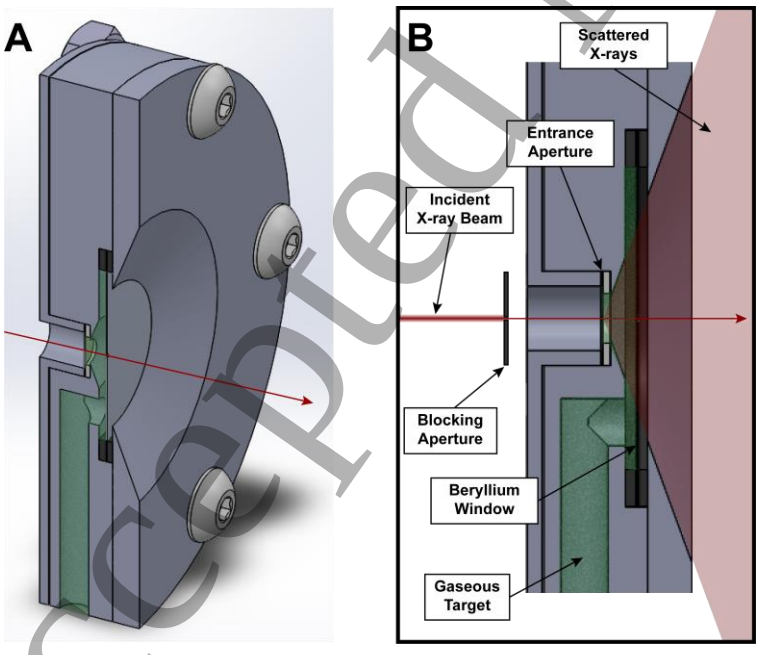

Figure 2. (A) Full cross-section of the scattering cell. The x-ray beam propagation axis is indicated in red, and the gaseous target is represented as a green shaded region. (B) A close-up cross-section of the interaction region, with relevant components labeled.

The gas cell is constructed of stainless steel with a 3.2 mm ID inlet tube for the gaseous target molecule (see Figure 2). The cell has a 2.4 mm pathlength and is constructed with a 250 μm platinum entrance aperture on the upstream side and a beryllium exit window with a 250 μm aperture on the downstream side. These hole

sizes were carefully chosen to avoid obstruction of the primary x-ray beam while allowing for sufficient gas flow between x-ray pulses (see below).

In order to prevent Bragg scattering of the primary x-ray beam from the inside of the cell entrance aperture, an upstream blocking aperture is used (see Figure 2B). The upstream blocking aperture has a 200 μm diameter opening, which allows the vast majority of the primary x-ray beam (focused to nominally 30 μm FWHM) to pass while blocking the low-intensity "edges" of the incident beam. This inevitably causes Bragg scattering from the platinum metal, which is subsequently blocked from entering the interaction region by the scattering cell itself. The entrance aperture, which has a 250 μm diameter opening, then allows the primary x-ray beam to pass cleanly to the interaction region. The diffuse scatter from the blocking aperture that enters the cell through the entrance aperture is weak and occurs at such a small scattering angle that it is not detected in this experiment.

The cell was designed for unobstructed observation of scattering at angles up to ~60°. A very thin (100 μm) disk of beryllium was chosen as the exit window material because it is nearly transparent to x-rays (98.8% transparency at 9.5 keV[36]). There is a very small dependence of the transmission on the scattering angle due to the changing pathlength. This effect is on the order of 0.5% in the absolute scattering signal, but is canceled out when analyzing the percentage change in the signal as described in Section 2.4.

A relatively small pathlength of the interaction region, 2.4 mm, was chosen for two reasons. Firstly, the short interaction length limits the Beer-Lambert attenuation of the UV pump pulse as it propagates through the sample. During the pump-probe experiments, it is necessary to have a significant number of excited molecules (as this is the signal being measured) but to avoid an excitation probability larger than about 10% at any point in the interaction region (to minimize multiphoton absorption). To attain both of these conditions, a near-constant excitation probability of less than 10% is desired. To achieve this, the Beer-Lambert attenuation is offset by weakly focusing the pump beam at the downstream end of the cell as detailed in a previous article[19]. The short interaction length, in concert with careful control of the gas pressure and UV intensity, helps to ensure that the desired balance is achieved. The evaluation of the optimal sample pressure is described in Section 2.3.

The other benefit of a short interaction length is that it allows good resolution of the scattering angle. With any finite interaction length, there is an inherent limit on scattering angle resolution caused by scattering from molecules at the upstream and downstream ends of the interaction region reaching the same point on the detector. The effect depends on the radial distance of the detection point from the beam propagation axis. At 9.5 keV x-ray energy and an 86 mm sample-to-detector distance (determined via calibration as described in Section 2.2), the q resolution is ~0.06 $Å^{-1}$ or better over the range of detection.

The sizes of the entrance and exit apertures (both 250 μm) were chosen to not only allow the pump and probe pulses to pass through, but also to allow sufficient flow for proper sample turnover between x-ray pulses. Given that the sample cell is placed inside a vacuum chamber with 2000 L/s turbomolecular pumps, we can use the approximation that the pressure outside the cell is negligible relative to the pressure inside. Thus, we can calculate the flow rate q_{cell} out of the cell as[37]:

$$q_{cell} = P_{cell} \cdot (A_{entrance} + A_{exit}) \cdot \sqrt{\frac{k_B T}{2\pi m}} \quad (10)$$

where P_{cell} is the pressure inside the cell, $A_{entrance}$ and A_{exit} are the areas of the respective apertures, k_B is the Boltzmann constant, T is the temperature, and m is the molecular mass. Using 7 Torr of N-methyl morpholine at 22°C, q_{cell} = 0.0427 Torr·L/sec. This implies that the gas in the cell, with volume V_{cell} ~ 0.3 mL, will turn over every ~50 milliseconds, or about every sixth x-ray pulse. It also implies that the product of pressure times pathlength from the gas inside the cell is about four orders of magnitude larger than from the background gas in the experimental chamber.

The region where the laser pulse and the x-ray pulse both interact with the molecules is a very small portion of the total cell volume. It is thus informative to consider the motion of individual molecules as opposed to the collective flow of the ensemble. The root mean-square distance traveled between x-ray shots on account of diffusion of molecules in the gas is

$$\langle x^2 \rangle^{1/2} = \sqrt{\frac{2\lambda v}{3f}} \quad (11)$$

where λ is the mean free path, v is the average thermal particle velocity, and f is the repetition rate of the experiment. Using 7 Torr of N-methyl morpholine at 22°C with the LCLS operating at 120 Hz, and estimating a collision cross section of 1 nm^2, $\langle x^2 \rangle^{1/2} \approx 2.0$ mm. Given that the diameter of the x-ray spot is only 30 μm FWHM, the probability of scattering off of the same molecule with multiple x-ray pulses is negligible.

2.2 Calibration of the detector distance

To properly calibrate the measured absolute scattering signals, it is necessary to consider the physical geometry of the detector relative to the interaction region. Scattering patterns calculated from classical Thomson scattering equations[28] represent the scattering per unit area as a function of 2θ at a fixed distance R between the scattering medium and the point of detection. In experiments employing a planar detector, the detector is usually positioned perpendicularly to the primary x-ray beam axis. Thus, the distance R is not constant, and geometric correction factors must be applied for direct comparison to the calculated scattering patterns. The measured intensity is divided by a $cos\,(2\theta)^{\,2}$ factor to correct for the R dependence. The measured intensity is also divided by an additional $\cos(2\theta)$ factor to normalize for the effective area of pixels at different displacements from the beam axis. Combined, the measured scattered intensity is divided by $cos\,(2\theta)^3$ to compare with calculated scattering patterns.

The patterns used for detector calibration are generated from calculated ground-state molecular structures using the Independent Atom Model**Error! Bookmark not defined.**, which is reasonable for ground-state molecular structures[28,38]. The X-rays produced by LCLS are linearly polarized, for which the scattering signal of Equation 2 takes the form

$$I_{scatt}(\theta, 2\theta) = \left(\frac{d\sigma_{Th}}{d\Omega}\right) \cdot \frac{I_0}{R^2} \cdot (sin^2\,\phi + cos^2\,\phi\, cos^2\,2\theta) \quad (12)$$

Here, the polarization factor depends on the scattering angle 2θ as well as the azimuthal angle with respect to the X-ray polarization, ϕ. Once these correction factors are applied to the theoretical patterns, comparison of the two-dimensional images can yield the precise distance and orientation of the detector relative to the interaction region.

The detector used is a planar 2.3-megapixel Cornell-SLAC Pixel Array Detector (CSPAD)[39] with a known internal pixel geometry. A least-squares optimization is performed between the image generated from a calculated optimized molecular geometry and the experimentally measured ground-state scattering pattern. The optimization outputs four geometrical parameters: x_0, y_0, and z_0 are the absolute geometrical coordinates of the center of the detector relative to the interaction region, assuming that the detector plane is perpendicular to the x-ray beam; and ϕ_0 is the azimuthal angle of the detector relative to the x-ray polarization. The optimization also includes an overall intensity scaling factor. The scattering angles θ and ϕ are related to x_0, y_0, and z_0 as follows:

$$\theta = \frac{1}{2}\tan^{-1}\frac{\sqrt{{x_0}^2 + {y_0}^2}}{z_0} \quad (13)$$

$$\phi = arctan2(y_0, x_0) + \phi_0 \quad (14)$$

By performing this optimization with ground-state scattering patterns, for which optimized geometries can be calculated reliably, we ensure that the measured excited-state patterns are also properly calibrated. Results of this calibration using N-methylmorpholine are shown in Figure 3. Repeated determinations of the sample-to-detector distance z_0 indicate that this value is determined with a standard deviation of less than 2 mm (less than 2% of the determined value). This standard deviation is less than the pathlength of the interaction region (2.4 mm), and yields scattering patterns in excellent agreement with theory, as shown in Figure 6.

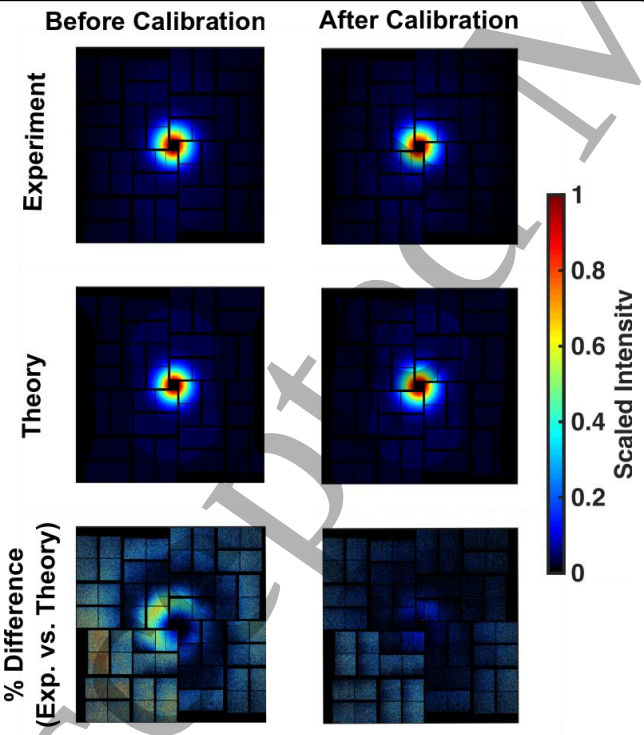

Figure 3. Comparison of experimental and calculated two-dimensional scattering patterns of ground-state N-methylmorpholine. Also shown are the fit residuals in the form of percent difference.

2.3 Sample delivery & optimization

The gas pressure in the sample cell must be carefully chosen in order to obtain the optimal signal to noise ratio for the pump-probe scattering experiment. The total scattering signal scales linearly with the

gas pressure, so that for gas phase structure determinations higher pressures are always desirable. In pump-probe experiments with optical excitation, however, the sample can attenuate the laser beam as it traverses the interaction region. Downstream molecules are exposed to less laser radiation, leaving them with a reduced level of optical excitation. The scattering signal from those downstream molecules therefore does not contain as much pump-probe signal while still contributing to the total scattering signal and therefore to the noise of the measurement. It is not advisable to make up for that by increasing the optical pump pulse energy because that would more likely lead to undesired multi-photon processes that populate higher states, with unknown effects on the molecular dynamics.

The attenuation of the optical pulse intensity as it propagates through the cell is partially combatted by focusing the laser beam toward the downstream end of the scattering cell. As the laser pulse traverses the sample, the loss of pulse energy is compensated for by a reduced laser beam area, keeping the laser intensity more level. Nevertheless, the signal-to-noise ratio of the pump-probe experiment can be optimized by carefully adjusting the gas pressure. To analytically reproduce that observation, we treat the pump-probe scattering signal while making the following assumptions: the x-ray and laser beams are perfectly overlapped; the laser beam has a uniform radial intensity profile (i.e. we ignore the focusing); within the sample cell, the sample molecular number density ρ_0 is constant over the sample cell with path length l; the x-ray beam is not attenuated as it propagates through the sample; and the sample cell length is small so that the q-dependent scattering signals from each point in the cell are indistinguishable.

As the laser and x-ray beams propagate through the sample, the optical laser intensity decreases. The scattering signal from an infinitesimally small region on the beam paths can be written as:

$$dP(x, q, \Delta q) = \sigma_x(q, \Delta q) \cdot P_0 \cdot \rho(x) dx \tag{15}$$

where all the molecule-dependent scattering terms are combined into a q-dependent scattering cross section $\sigma_x(q, \Delta q)$. The number of incoming x-ray photons, P_0, may be taken on a per-pulse or on a per-unit-time basis. Here we also replace the number of irradiated molecules divided by the x-ray beam area, N/A_0, by the molecular number density times the infinitesimal path length $\rho(x)dx$. With the pump laser beam off, the signal integrated over the cell path length l becomes:

$$P_{off}(q, \Delta q) = \int_0^l \sigma_{x,gr}(q, \Delta q) \cdot \rho_0 \cdot P_0 \, dx = \sigma_{x,gr}(q, \Delta q) \cdot \rho_0 \cdot P_0 \cdot l \tag{16}$$

where ρ_0 is the molecular number density that is to be optimized and $\sigma_{x,gr}(q, \Delta q)$ is the scattering cross section of the ground state molecules.

For the signal with the pump laser on, the density of excited state molecules $\rho_{exc}(x)$ and the density of ground state molecules $\rho_{gr}(x)$ depend on the position x along the beam path, so that the pump-laser on signal becomes:

$$P_{on}(q, \Delta q) = \int_0^l \left(\sigma_{x,exc}(q, \Delta q) \cdot \rho_{exc}(x) \cdot P_0 + \sigma_{x,gr}(q, \Delta q) \cdot \rho_{gr}(x) \cdot P_0\right) dx \tag{17}$$

The density of excited states arising from optical excitation is given, for linear processes, by:

$$\rho_{exc}(x) = \rho_0 \cdot \sigma_{opt} \cdot I_{opt}(x) \tag{18}$$

where σ_{opt} is the optical absorption cross section and $I_{opt}(x)$ is the path-dependent intensity of the optical laser. The latter is given by the Beer-Lambert law[40] as:

$$I_{opt}(x) = I_{opt,0} \cdot e^{-\sigma_{opt} \cdot \rho_0 \cdot x} \tag{19}$$

The density of ground state molecules is just the sample pressure density ρ_0 minus the excited state density, so that the laser-on signal integrates to:

$$P_{on}(q, \Delta q) = \left(\sigma_{x,exc}(q, \Delta q) - \sigma_{x,gr}(q, \Delta q)\right) \cdot P_0 \cdot I_{opt,0} \cdot \left(1 - e^{-\sigma_{opt} \cdot \rho_0 \cdot l}\right) + \sigma_{x,gr}(q, \Delta q) \cdot \rho_0 \cdot P_0 \cdot l \tag{20}$$

The experimentally measured percent difference signal then becomes:

$$\frac{P_{on}(q, \Delta q) - P_{off}(q, \Delta q)}{P_{off}(q, \Delta q)} = \frac{\left(\sigma_{x,exc}(q, \Delta q) - \sigma_{x,gr}(q, \Delta q)\right)}{\sigma_{x,gr}(q, \Delta q)} \cdot I_{opt,0} \cdot \frac{\left(1 - e^{-\sigma_{opt} \cdot \rho_0 \cdot l}\right)}{\rho_0 \cdot l} \tag{21}$$

It is clear that larger changes in the molecular scattering signals upon optical excitation lead to increased percent difference signals. It is also evident that increasing the intensity of the incoming optical pump radiation, $I_{opt,0}$, benefits the observed signal. This is only true to some extent, however: in order to minimize the probability of multi-photon processes, the pump laser intensity needs to be kept low. In general, higher order photoexcitation processes are associated with 2-photon, 3-photon or higher cross sections, which are generally not known. In practice, one therefore aims to keep the probability of 1-photon optical excitation low, in order to minimize the occurrence of higher order processes (see also discussion in Section 3).

The probability of optical excitation, at the entrance of the cell before the laser is attenuated, is:

$$\mathbb{P} = \sigma_{opt} \cdot I_{opt,0} \tag{22}$$

so that the incoming optical radiation intensity is limited to:

$$I_{opt,0} = \frac{\mathbb{P}_{max}}{\sigma_{opt}} \tag{23}$$

where $\mathbb{P}_{max}$ is the maximum allowable optical excitation probability. In our experiments we have aimed to keep $\mathbb{P}_{max}$ to less than 10%. The percent difference signal then becomes:

$$\frac{P_{on}(q, \Delta q) - P_{off}(q, \Delta q)}{P_{off}(q, \Delta q)} = \frac{\left(\sigma_{x,exc}(q, \Delta q) - \sigma_{x,gr}(q, \Delta q)\right)}{\sigma_{x,gr}(q, \Delta q)} \cdot \frac{\mathbb{P}_{max}}{\sigma_{opt}} \cdot \frac{\left(1 - e^{-\sigma_{opt} \cdot \rho_0 \cdot l}\right)}{\rho_0 \cdot l} \tag{24}$$

which reveals that, somewhat counter-intuitively, molecular systems with larger optical absorption cross section give rise to smaller pump-probe signals. It therefore is wise to choose systems with small absorption cross sections, provided enough pump laser intensity is available to reach the maximum excitation probability.

In many experiments shot noise, which can be approximated by the square root of the signal counts, is the dominant source of noise. In many experimental procedures, pump laser-on and pump laser-off patterns are measured for each time step, so that many more laser-off patterns are accumulated. Consequently, the noise, which we express as Δ, is dominated by the noise in the laser-on patterns:

$$\Delta \frac{P_{on} - P_{off}}{P_{off}} = \frac{\Delta P_{on}}{P_{off}} = \frac{\sqrt{P_{on}}}{P_{off}} \tag{25}$$

The change in the scattering signals upon optical excitation is often small, so that the noise can be approximated by $1/\sqrt{P_{off}}$. With (14) and (22) we obtain for the signal-to-noise ratio:

$$S/N = \frac{\left(\sigma_{x,exc}(q,\Delta q) - \sigma_{x,gr}(q,\Delta q)\right)}{\sqrt{\sigma_{x,gr}(q,\Delta q)}} \cdot \frac{\mathbb{P}_{max}}{\sigma_{opt}} \cdot \frac{\left(1 - e^{-\sigma_{opt}\cdot\rho_0\cdot l}\right)}{\sqrt{\rho_0 \cdot l}} \cdot \sqrt{P_0} \tag{26}$$

With the pump-probe scattering signals and optical absorption cross section determined by the molecular system, and the maximum allowable excitation probability $\mathbb{P}_{max}$ constrained as discussed, very few handles lend themselves to optimization. Increasing the number of x-ray photons, P_0, is the obvious route, but limits arise from the x-ray source and the allocated beam time. As x-ray sources such as LCLS-II and the European XFEL offer higher repetition rates, this limitation will be improved. Nevertheless, the S/N depends sensitively on the sample pressure (proportional to the product of the sample number density times cell length, $\rho_0 \cdot l$), as shown in Figure 4. The maximum is at:

$$(\rho \cdot l)_{opt} \approx \frac{1.256}{\sigma_{opt}} \tag{27}$$

The optimal vapor pressure is independent of the other parameters, including the chosen maximum excitation probability. It is only a function of the cell length l and the optical absorption cross section σ_{opt}. Weakly absorbing samples allow using a higher vapor pressure, which is advantageous for the signal and the signal-to-noise ratio.

For the experiments on N-methyl morpholine[7], the cell path length is $l = 0.24\,cm$ and the optical absorption cross section at 200 nm is $\sigma_{opt} = 1.5 \cdot 10^{-17}\,cm^2$. This suggests that the optimal sample density is $(\rho)_{opt} \approx 3.4 \cdot 10^{17}\,cm^{-3} \approx 10\,Torr$.

Importantly, as Figure 4 shows, the signal quickly declines if the sample pressure is not optimal. In our experiments we optimize the signal-to-noise ratio for each molecular compound before taking long runs of data. In NMM the optimization resulted in a best sample pressure of 7 Torr. The agreement between the calculated optimum, 10 Torr, and the measured optimum, 7 Torr, is satisfactory in light of the previously stated assumptions. In addition, the sample cell is windowless, so that gas streams out of the cell. This vapor can absorb the laser beam before it enters the cell, and since the platinum apertures block the x-ray scattering from that region, no

corresponding pump-probe signal is observed. Rough estimates of an effusive gas flow out of the sample cell indicate that indeed, this initial absorption can account for much of the observed discrepancy.

2.4 Data processing

Using the LCLS x-ray free electron laser for ultrafast time-resolved scattering experiments has many advantages such as short pulse duration and high photon flux. But it also creates distinct challenges. The SASE pulses at LCLS have significant shot-to-shot fluctuations in pulse arrival time, pulse intensity, and beam pointing. In order to achieve a high signal-to-noise ratio these fluctuations must be accounted for.

In time-resolved experiments, the relative timing of the pump and probe pulses is controlled via a motorized delay stage. In addition, we also monitor the timing jitter via a spectrally encoded cross-correlator that has been described in detail elsewhere[41]. Briefly: a chirped while light continuum is directed through a thin silicon nitride film, and then dispersed onto a CCD camera as a reference spectrum. Then, the chirped white light is crossed with the x-ray pulse on the film. The x-ray pulse changes the index of refraction of the silicon nitride, causing a drop in transmission. The measured spectrum is then subtracted from the reference spectrum, resulting in a sharp decrease in intensity at a given point in the measured frequency spectrum. After calibrating the position of the edge as a function of x-ray pulse arrival time, this “time tool” can be used as a shot-to-shot measure of the timing jitter.

Although LCLS boasts x-ray pulse durations as short as 10 fs, the time resolution in this experiment is limited by the pulse duration of the exciting optical pulse and the jitter between optical and x-ray pulses. In our experiments, the actual temporal profiles of the x-ray and optical pulses have not been measured. Estimates of the overall time resolution of the experiment have instead been derived from the molecular response to photoexcitation, which varies for each molecular system. Development of an autocorrelator for future optical pulse characterization is currently underway.

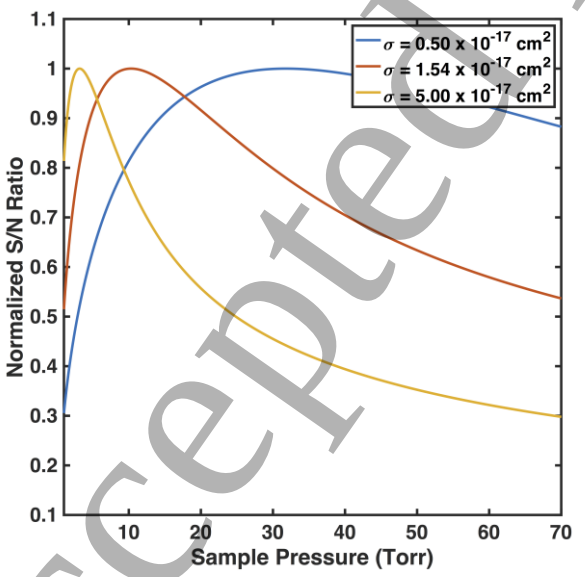

Figure 4. The dependence of the overall signal-to-noise ratio on the sample pressure and the optical cross-section σ for a 2.4 mm optical path length, for select optical absorption cross sections as noted in the legend.

In the experiments employing the re-designed scattering cell described in section 2.1, fluctuations in x-ray intensity incident on the sample arises from two sources: the fluctuations in total pulse-to-pulse x-ray intensity; and the spatial pointing instability of the x-ray beam, which affects transmission through the blocking and entrance apertures. In order to simultaneously correct for both effects, the transmitted x-ray intensity through the sample is monitored with a photodiode downstream of the CSPAD. The single-shot x-ray scattering patterns are then corrected for

the photodiode value prior to averaging.

As shown in Figure 5, the downstream photodiode reading scales quite linearly with the overall integrated intensity of the CSPAD for ground-state molecular scattering. However, as molecular structures change in electronically excited states, the fraction of total scattered photons that are actually detected will change, and so the integrated CSPAD intensity cannot be used as a reliable measure of incident x-ray intensity. Thus, the photodiode reading was found to be a suitable replacement.

It should be noted that this method assumes that the transmitted x-ray intensity is independent of the molecular dynamics. This is a reasonable approximation, as the total number of scattered photons is a very small fraction of the total number of incident photons. The total transmitted intensity therefore is a very good representation of the total incident intensity, and can be used for calibration.

Once the scattering images have been corrected for both intensity and timing jitter, the time-dependent signals are expressed as a percent difference, Equation 1. As previously discussed, this treatment eliminates experimental artifacts that equally affect both the UV-on and UV-off scattering signals. Such factors include the previously discussed $\cos^3(2\theta)$ term used to correct for detector planarity (see Section 2.2), and the x-ray polarization factor (see Equation 12). These terms are important for comparing absolute scattering signals, but ultimately do not affect difference signals.

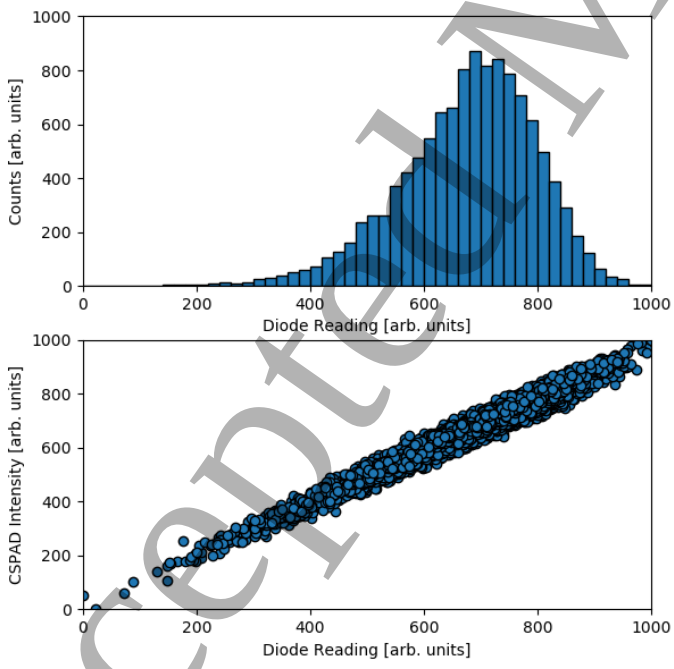

Figure 5. (Top) Histogram of the downstream photodiode reading over ~12,000 x-ray shots from LCLS operating at 9.5 keV photon energy. (Bottom) Plot of the downstream photodiode reading vs. integrated CSPAD intensity for the same ~12,000 x-ray shots. The scattering target was ground-state dimethyl piperazine.

Expressing the measured signals as a percent difference also eliminates several other scattering angle-dependent factors. Attenuation of the scattered x-rays by the beryllium exit window varies with scattering angle as the effective pathlength of solid beryllium changes. Given the exceptional transparency of beryllium to hard x-rays (100 μm thick Be is 98.8% transparent at 9.5 keV) and the very thin (100 μm) window used, this effect is very small (~0.5%) in the absolute scattering patterns. Even so, time-dependent changes in scattering signal are often of small magnitudes, and so eliminating this effect is a necessary step. Other scattering-angle dependent factors include any variations in pixel responsiveness in different regions of the detector.

It should also be noted that there

are several other relevant scattering-angle dependent factors that do not cancel out when taking the percent difference and must be mitigated otherwise. Such factors include any background scattering, which is additive, and so it is eliminated in the numerator of Equation 1, but remains in the denominator. For this reason, the recent re-design of the scattering cell included a blocking aperture that significantly decreased background signals (see Figure 6). In addition, any time-dependent fluctuations in x-ray intensity are not removed via this data treatment, which necessitates the external intensity calibration via a photodiode described above. Also, any effects arising from the introduction of the optical laser (polarization effects, intensity fluctuations, changes in UV/x-ray spatial overlap, etc.) remain, and must be minimized to the extent possible.

To further improve the signal-to-noise ratio of the measured scattering images, the four "quadrants" of the scattering image are also averaged. Because of the inversion symmetry caused by the linear polarization of the x-ray beam[13] (Equation 12), each "quadrant" of the scattering image contains identical structural information. Thus, the redundant quadrants can be averaged to reduce the overall noise.

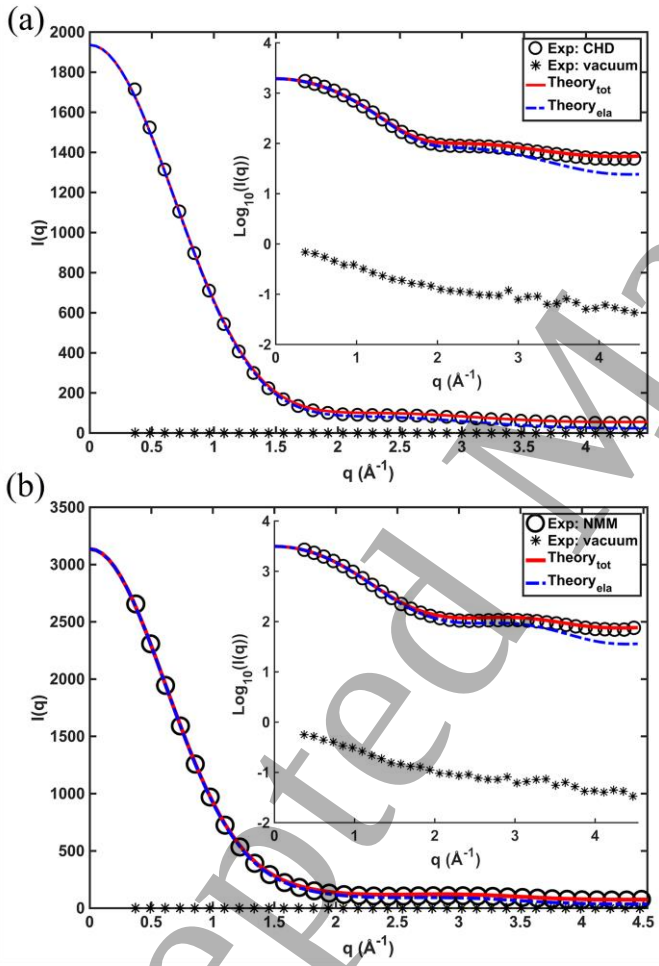

Figure 6. Comparison between experimental and theoretical scattering patterns on absolute and logarithm scales (insert) for (a) 1,3-cyclohexadiene (CHD) and (b) N-methylmorpholine (NMM). Theory$_{tot}$ and Theory$_{ela}$: theoretical total and elastic x-ray scattering patterns calculated by ab initio wavefunctions[44] (CAS(6,6)/6-311++G(d,p) for CHD, CAS(6,4)/6-311++G(d,p) for NMM). Experimental backgrounds when there is no gas in the interaction region are shown as "Exp: vacuum". Scale factors were applied to the experimental patterns to make them comparable to the theoretical ones.

Finally, in order to develop a q-dependent estimate of the shot noise for each measured pattern, the total number of measured photons incident on each part of the detector was estimated. This was performed by first creating a histogram of the detector response value (measured in analog-to-digital units, ADU) across the detector over thousands of x-ray shots. From this analysis of the pixel response, the average ADU per photon was determined. In this way, the total detector response in ADU was divided by this average value as an estimate of the total number of photons collected at all points in the image. Approximating the shot noise as the square root of the total number of measured photons then provided error bars for the measured signals.

3. Results and discussion

The careful optimization of the wide range of experimental factors discussed in Section 2 yielded scattering patterns with exceptionally low noise and negligible background scatter (see Figure 6). This exceptional data quality has recently revealed intricate details of a variety of molecular processes. In 2018, using N-methylmorpholine (NMM) as a model system, excited-state x-ray scattering patterns were used to identify the excited electronic state via its transition dipole moment[13]. Shortly afterward, analysis of the time-dependent scattering signals of NMM following photoexcitation revealed coherent vibrations that dephase on a picosecond time scale[7]. Recently, similar experiments also revealed multiple competing pathways in the UV-induced photodissociation of trimethylamine[42] and an array of insights into the initial electronic redistribution[14], structural dynamics[45], and product species formed[43] following deep-UV excitation of CHD. Of course, correct interpretation of all these data sets rests on carefully treated experimental and theoretical scattering signals, as discussed in detail in previous sections.

Serving as the reference signal in pump-probe x-ray scattering experiments, the precise measurement of ground-state x-ray scattering pattern is essential and provides the foundation for accurate interpretation of the observed structural dynamics. Inaccurate reference signals can lead to erroneous determinations of excited state molecular structures, molecular motions and reaction pathways. To evaluate the quality of the measured reference signals, Figure 6 shows two experimental ground-state x-ray scattering signals. These signals were used as reference signals for ultrafast x-ray scattering experiments of CHD[45] and NMM[7], respectively. Important data processing steps such as pulse-to-pulse scattering intensity calibration, detector distance calibration, geometric correction factor and x-ray polarization factor described in the previous sections have all been applied to the experimental laser-off scattering patterns shown in Figure 6, making them directly comparable to the calculated scattering patterns derived from high level *ab initio* wavefunctions. The agreement between the experimental and theoretical scattering curves is excellent for both systems. A careful examination of the logarithmic plots manifests the inadequate descriptions of the measured scattering signals if only elastic scattering is considered, emphasizing the importance of including inelastic scattering, e.g. Compton scattering, in the total x-ray scattering signals. The experimental "vacuum" curves shown in the figure are measured and processed under the same conditions except that there is no gas in the interaction region. The fact that the backgrounds are reproducible and consistently about more than three orders smaller than the experimental curves affirms the quality of the reference signals. This precise data treatment allows not only for determination of ground-state molecular structures, but also those in electronically excited states. Following the dephasing of coherent vibrations initiated via excitation to the 3p molecular Rydberg state, NMM gives constant scattering signals arising from the excited-state molecular structure. By fitting the measured signal at long delay time to those generated from a pool of calculated structures (as described in detail in Reference 7), the interatomic distances in the excited-state are determined (see Table 1).

By performing this fitting independently for each of 25 measured time points, the standard deviation in each geometric parameter is determined. It should be noted that the standard deviations in the determined distances shown in Table 1 are a measure of the precision of the

	C1	C2	C3	C4	C5	N	O
C1		1.578 ± 0.023 1.580	2.307 ± 0.015 2.345	2.837 ± 0.013 2.864	3.682 ± 0.058 3.493	2.497 ± 0.028 2.433	1.364 ± 0.008 1.401
C2			2.846 ± 0.021 2.864	2.367 ± 0.026 2.433	2.513 ± 0.021 2.525	1.441 ± 0.019 1.439	2.491 ± 0.026 2.425
C3				1.557 ± 0.009 1.580	3.648 ± 0.057 3.493	2.480 ± 0.036 2.433	1.368 ± 0.005 1.401
C4					2.542 ± 0.039 2.525	1.434 ± 0.012 1.439	2.486 ± 0.020 2.425
C5						1.433 ± 0.007 1.454	4.189 ± 0.053 4.015
N							2.880 ± 0.022 2.762
O							

Table 1. Experimentally determined molecular structure parameters (black) of NMM in the 3s molecular Rydberg state, determined for delay times from 2.6 ps to 3.9 ps. Errors displayed are the standard deviations over measurements at different time points. For comparison, the structure parameters from the calculated geometry in the cationic ground state are shown in blue below the experimental values.

result, rather than the overall accuracy. As the calculation of structures in highly excited electronic states of polyatomic molecules is unreliable, theoretical results cannot be used as absolute benchmarks. For an approximate comparison, the interatomic distances calculated for the electronic ground state of the NMM^+ cation (calculated with B3LYP/6-311++G(d,p)) are included in Table 1. We note that the structure of NMM in the molecular Rydberg state is not necessarily identical to the structure in the ion state, but they are likely rather similar. The good agreement between the experimental data for the Rydberg state and the computational data for the ion state suggests a good accuracy of the experimentally determined structure. Of course, any error in the determined sample-to-detector distance (as discussed in Section 2.2) would also affect the accuracy of the determined excited-state structures. The estimated uncertainty of ~2% in the detector distance has been simulated to affect the nearest-neighbor interatomic distances by ~1% (~0.01Å). Still, the good agreement of the ground-state scattering patterns with theory suggests that the excited-state patterns are of similar quality.

The ultrafast pump-probe x-ray scattering experiments using the implementation in this article mostly studied the molecular dynamics of one-photon excitation[7,13,14,45]. Since multi-photon excitation could lead to unwanted process such as ionization in the molecules, the excitation fractions were controlled to be low (< 10%). However, as multi-photon cross sections are not known, there could be a possibility that a small fraction of molecules absorb two (or more)

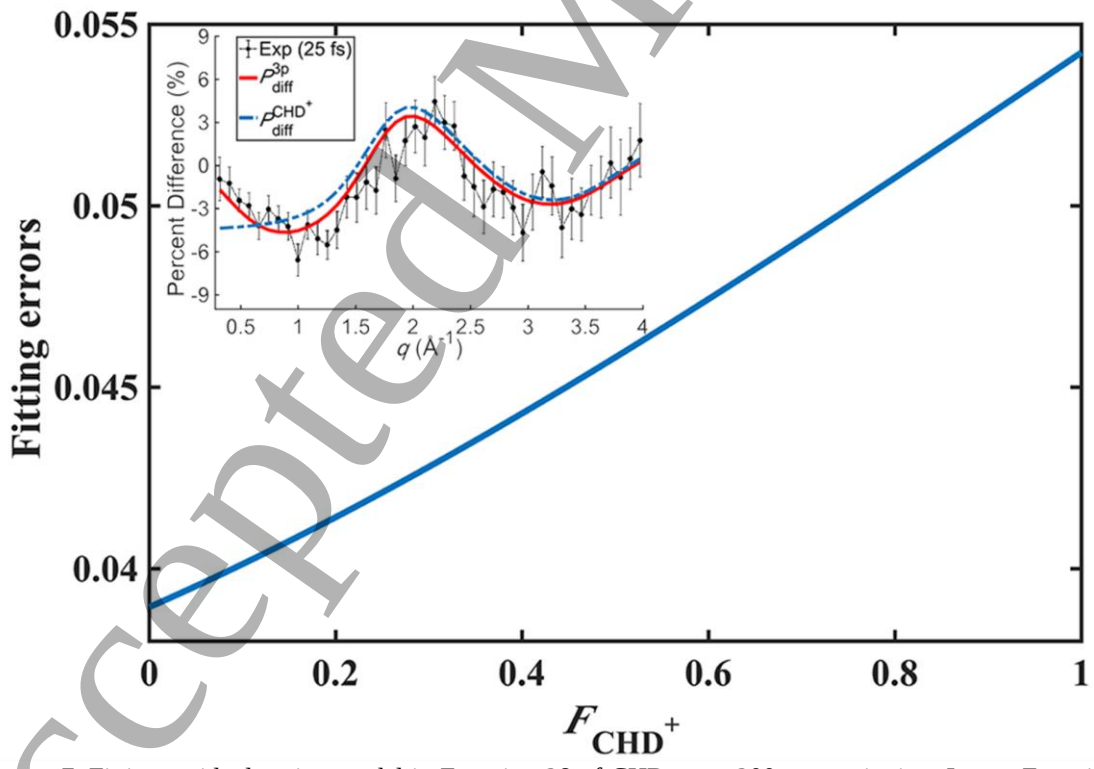

Figure 7. Fitting residuals using model in Equation 28 of CHD upon 200 nm excitation. Insert: Experimental and theoretical percent difference signals, $P_{diff}(q)$, assuming 100% excitation fraction adopted from Ref 14. Exp (25 fs): the experimental signal $P^{exp}_{diff}(q)$ divided by excitation fraction γ at 25 fs delay time with 1σ error bars. P^{3p}_{diff}: signal for the electronic 3p state. $P^{CHD^+}_{diff}$: signal for the CHD cation and one ionized electron.

photons, which would affect the interpretation of the scattering data. To rule out this possibility, we analyzed a previously published experimental data set that reported a direct measurement of the initial redistribution of electron density when the molecule 1,3-cyclohexadiene (CHD) is optically excited with a 200 nm laser[14]. Since the experimental signal from electron redistributions is very weak, any interfering signals from multi-photon excitation, if present, would likely become apparent in the analysis.

Considering that the energy of two photons at 200 nm is larger than the ionization energy of CHD, two-photon excitation could ionize the molecule, which would lead to the CHD cation. (Two-photon absorptions leading to superexcited, neutral molecules are possible, but the cross sections for such processes are smaller than the ionization cross sections.[46,47]) Even though the excitation fraction in this experiment was determined to be small (6%), we wish to further examine here the possibility of CHD cation formation from 2-photon ionization. To do so, we analyze the data specifically allowing for some of the molecules to be ionized from the optical excitation. If that were to happen, the experimental signal would be comprised of two parts, one part being the scattering signal caused by molecules that are excited to the 3p state, and another part from molecules that absorb two photons to become positive ions. We use the following model to fit the experimental scattering pattern (the black dots in Figure 7 insert):

$$P_{diff}^{\exp}(q) = \gamma \cdot \left((1 - F_{\mathrm{CHD}^+}) \cdot P_{diff}^{3p}(q) + F_{\mathrm{CHD}^+} \cdot P_{diff}^{\mathrm{CHD}^+}(q) \right) \quad (26)$$

where $P_{diff}^{3p}(q)$ is the percent difference scattering pattern of 3p excited CHD (the red curve in Figure 7 insert), $P_{diff}^{\mathrm{CHD}^+}(q)$ is the percent difference scattering pattern of the CHD cation and one free photoelectron (the dashed blue curve in Figure 7 insert), and F_{CHD^+} is the fraction of molecules that undergo two-photon excitation process. The excitation fraction is denoted as γ. We allowed both γ and F_{CHD^+} to vary from 0 to 100% independently. The resulting fitting residuals with respect to F_{CHD^+} are shown in Figure 7, where the minimum mean square root of the least-square fitting residuals at optimal γ values are plotted versus the F_{CHD^+} value. We find that a global minimum exists with F_{CHD^+}= 0.0% and γ=6.0%. This implies that no admixture of signal from ionized molecules would improve the fit of the data, which is consistent with the findings in Ref 14. Thus, this further analysis of the data confirms that two-photon excitation processes are, under the current experimental conditions, not likely and consequently unobservable within the current detection limit. As an aside, we point to an interesting recent paper by Bucksbaum et al. that intentionally exploits multiphoton induced excitation to study linear and nonlinear processes in the iodine molecule using time-resolved X-ray scattering[11].

4. Summary

Ultrafast time-resolved x-ray scattering is an exciting new technique to study chemical reaction dynamics. Enabled by a new generation of XFELs, deep data sets can be obtained that are rich in molecular detail. Scattering patterns are found to be excellently reproducible, and exquisitely sensitive to the nature of the optically excited state, the geometrical structure of molecules in excited states, and the changes in electron density distribution upon optical excitation. With a time resolution rivaling the best spectroscopic experiments, novel dynamics phenomena can now be explored.

This article describes a fully re-designed windowless diffractometer with blocking apertures that significantly reduces the intensity of background scattering signal in gas-phase experiments performed at LCLS. This scattering cell design offers inherent advantages over earlier designs, as it is fully in-vacuum, and provides for precise control of the sample pressure so that the signal-to-noise ratio of the measured pump-probe signal can be optimized. Implementation in a vacuum chamber is important because it minimizes unwanted background signals that hinder a fully quantitative analysis. This improved design, coupled with advances in intensity and geometry calibration, provided exceptionally low-noise scattering patterns that have revealed many subtle details of chemistry in excited states[7,14,45].

We demonstrate excellent agreement between measured patterns and *ab-initio* calculated total scattering signals for ground-state molecules, and we show that careful optimization of the optical excitation conditions successfully avoids any multi-photon processes.

These advances help broaden the applicability of ultrafast gas-phase x-ray scattering to an even wider range of chemical systems, including those that have very small expected changes in their scattering signal. This progress, coupled with the promise of improved repetition rate, photon energy, and time resolution at XFELs in the near future, is expected to lead to further exciting insights into ultrafast chemical reaction dynamics.

Acknowledgements

This project was supported by the U.S. Department of Energy, Office of Science, Basic Energy Sciences, under Award Nos. DE-SC0017995 and DE-SC0020276. N.G. acknowledges a graduate fellowship through the DOE Office of the Science Graduate Student Research (SCGSR) program.

References

[1] Zewail A H 2000 Femtochemistry: Atomic-Scale Dynamics of the Chemical Bond Using Ultrafast Lasers (Nobel Lecture) *Angew. Chem. Int. Ed.* **39** 2586–631

[2] Ischenko A A, Weber P M and Dwayne Miller R J 2017 Capturing Chemistry in Action with Electrons: Realization of Atomically Resolved Reaction Dynamics *Chem. Rev.* **117** 11066–124

[3] Ischenko A A, Weber P M and Miller R J D 2017 Transient Structures and Chemical Reaction Dynamics *Russ. Chem. Rev.* **86**

[4] Dudek R C and Weber P M 2001 Ultrafast diffraction imaging of the electrocyclic ring-opening reaction of 1,3-cyclohexadiene *J Phys Chem A* **105** 4167–71

[5] Minitti M P, Budarz J M, Kirrander A, Robinson J S, Ratner D, Lane T J, Zhu D, Glownia J M, Kozina M, Lemke H T, Sikorski M, Feng Y, Nelson S, Saita K, Stankus B, Northey T, Hastings J B and Weber P M 2015 Imaging Molecular Motion: Femtosecond X-Ray Scattering of an Electrocyclic Chemical Reaction *Phys. Rev. Lett.* **114** 1–5

[6] Wolf T J A, Sanchez D M, Yang J, Parrish R M, Nunes J P F, Centurion M, Coffee R, Cryan J P, Gühr M, Hegazy K, Kirrander A, Li R K, Ruddock J, Shen X, Vecchione T, Weathersby S P, Weber P M, Wilkin K, Yong H, Zheng Q, Wang X J, Minitti M P and Martínez T J 2019 The photochemical ring-opening of 1,3-cyclohexadiene imaged by ultrafast electron diffraction *Nat. Chem.* **11** 504–9

[7] Stankus B, Yong H, Zotev N, Ruddock J M, Bellshaw D, Lane T J, Liang M, Boutet S, Carbajo S, Robinson J S, Du W, Goff N, Chang Y, Koglin J E, Minitti M P, Kirrander A and Weber P M 2019 Ultrafast X-ray scattering reveals vibrational coherence following Rydberg excitation *Nat. Chem.* **21**

[8] Glownia J M, Natan a., Cryan J P, Hartsock R, Kozina M, Minitti M P, Nelson S, Robinson J, Sato T, van Driel T, Welch G, Weninger C, Zhu D and Bucksbaum P H 2016 Self-Referenced Coherent Diffraction X-Ray Movie of Ångstrom- and Femtosecond-Scale Atomic Motion *Phys. Rev. Lett.* **117** 153003

[9] Bennett K, Kowalewski M and Mukamel S 2017 Comment on Self-Referenced Coherent Diffraction X-Ray Movie of Ångstrom- and Femtosecond-Scale Atomic Motion *Phys. Rev. Lett.* **119** 1–2

[10] Glownia J M, Natan A, Cryan J P, Hartsock R, Kozina M, Minitti M P, Nelson S, Robinson J, Sato T, Van Driel T, Welch G, Weninger C, Zhu D and Bucksbaum P H 2017 Glownia et al. Reply *Phys. Rev. Lett.* **119** 153003

[11] Bucksbaum P H, Ware M R, Natan A, Cryan J P and Glownia J M 2020 Characterizing Multiphoton Excitation Using Time-Resolved X-ray Scattering *Phys. Rev. X* **10** 11065

[12] Yang J, Zhu X, Wolf T J A, Li Z, Nunes J P F, Coffee R, Cryan J P, Gühr M, Hegazy K, Heinz T F, Jobe K, Li R, Shen X, Veccione T, Weathersby S, Wilkin K J, Yoneda C, Zheng Q, Martinez T J, Centurion M and Wang X 2018 Imaging CF_3I conical intersection and photodissociation dynamics with ultrafast electron diffraction *Science.* **361** 64–7

[13] Yong H, Zotev N, Stankus B, Ruddock J M, Bellshaw D, Boutet S, Lane T J, Liang M, Carbajo S, Robinson J S, Du W, Goff N, Chang Y, Koglin J E, Waters M D J, Sølling T I, Minitti M P, Kirrander A and Weber P M 2018 Determining Orientations of Optical Transition Dipole Moments Using Ultrafast X-ray Scattering *J. Phys. Chem. Lett.* **9** 6556–62

[14] Yong H, Zotev N, Ruddock J M, Stankus B, Simmermacher M, Carrascosa A M, Du W, Goff N, Chang Y, Bellshaw D, Liang M, Carbajo S, Koglin J E, Robinson J S, Boutet S, Minitti M P, Kirrander A and Weber P M 2020 Observation of the molecular response to light upon photoexcitation *Nat. Commun.* **11**

[15] Yang J, Zhu X, F. Nunes J P, Yu J K, Parrish R M, Wolf T J A, Centurion M, Gühr M, Li R, Liu Y, Moore B, Niebuhr M, Park S, Shen X, Weathersby S, Weinacht T, Martinez T J and Wang X 2020 Simultaneous observation of nuclear and electronic dynamics by ultrafast electron diffraction *Science.* **368** 885–9

[16] Jiang Y, Liu L C, Sarracini A, Krawczyk K M, Wentzell J S, Lu C, Field R L, Matar S F, Gawelda W, Müller-Werkmeister H M and Miller R J D 2020 Direct observation of nuclear reorganization driven by ultrafast spin transitions *Nat. Commun.* **11**

[17] Harb M, Ernstorfer R, Hebeisen C T, Sciaini G, Peng W, Dartigalongue T, Eriksson M A, Lagally M G, Kruglik S G and Miller R J D 2008 Electronically driven structure changes of Si captured by femtosecond electron diffraction *Phys. Rev. Lett.* **100** 1–4

[18] Pemberton C C, Zhang Y, Saita K, Kirrander A and Weber P M 2015 From the (1B) Spectroscopic State to the Photochemical Product of the Ultrafast Ring-Opening of 1,3-Cyclohexadiene: A Spectral Observation of the Complete Reaction Path *J. Phys. Chem. A* **119** 8832–45

[19] Budarz J M, Minitti M P, Stankus B and Kirrander A 2016 Observation of femtosecond molecular dynamics via pump – probe gas phase x-ray scattering *J. Phys. B At. Mol. Opt. Phys.* **49** 34001

[20] Cardoza J D, Dudek R C, Mawhorter R J and Weber P M 2004 Centering of ultrafast time-resolved pump-probe electron diffraction patterns *Chem. Phys.* **299** 307–12

[21] Schülke W 2007 *Electron Dynamics by Inelastic X-Ray Scattering* (OUP Oxford)

[22] Als-Nielsen J and McMorrow D 2011 *Elements of Modern X-ray Physics* (Wiley)

[23] Santra R 2008 Concepts in x-ray physics *J. Phys. B At. Mol. Opt. Phys.* **42** 23001

[24] Popova-Gorelova D 2018 Imaging electron dynamics with ultrashort light pulses: A theory perspective *Appl. Sci.* **8**

[25] Dixit G, Vendrell O and Santra R 2012 Imaging electronic quantum motion with light *Proc. Natl. Acad. Sci. U. S. A.* **109** 11636–40

[26] Bennett K, Kowalewski M, Rouxel J R and Mukamel S 2018 Monitoring molecular nonadiabatic dynamics with femtosecond X-ray diffraction *Proc. Natl. Acad. Sci. U. S. A.* **115** 6538–47

[27] Simmermacher M, Henriksen N E, Møller K B, Moreno Carrascosa A and Kirrander A 2019 Electronic Coherence in Ultrafast X-Ray Scattering from Molecular Wave Packets *Phys. Rev. Lett.* **122** 73003

[28] Warren B E 1969 *X-ray Diffraction* (Courier Corporation)

[29] Ma L, Yong H, Geiser J D, Moreno Carrascosa A, Goff N and Weber P M 2020 Ultrafast x-ray and electron scattering of free molecules: A comparative evaluation *Struct. Dyn.* **7** 034102

[30] Doyle P A and Cowley J M 1973 *International Tables for X-Ray Crystallography* (Kynoch Press, Birmingham)

[31] Prince E 2006 International Tables for Crystallography. Vol. C: Mathematical, Physical and Chemical Tables, 3rd ed. (Springer, Dordrecht, The Netherlands).

[32] Debye P 1915 Zerstreuung von Röntgenstrahlen *Ann. Phys.* **351** 809–23

[33] Hubbell J H, Veigele W J, Briggs E A, Brown R T, Cromer D T and Howerton R J 1977 Erratum: Atomic Form Factors, Incoherent Scattering Functions, and Photon Scattering Cross Sections *J. Phys. Chem. Ref. Data* **6** 615–6

[34] Thakkar A J, Tripathi A N and Smith V H 1984 Molecular x-ray- and electron-scattering intensities *Phys. Rev. A* **29** 1108–13

[35] Zotev N, Moreno Carrascosa A, Simmermacher M and Kirrander A 2020 Excited Electronic States in Total Isotropic Scattering from Molecules *J. Chem. Theory Comput.* **16** 2594–605

[36] Henke B L, Gullikson E M and Davis J C 1991 X-ray interactions: photoabsorption, scattering, transmission, and reflection at E=50-30000 eV, Z=1-92 *Atomic Data and Nuclear Data Tables* **54** 181-342

[37] O'Hanlon J F 2005 *A user's guide to vacuum technology* (John Wiley & Sons)

[38] Hargittai I and Hargittai M 1988 *Stereochemical Applications of Gas-phase Electron Diffraction: Structural information for selected classes of compounds* (VCH)

[39] Philipp H T, Hromalik M, Tate M, Koerner L and Gruner S M 2011 Pixel array detector for X-ray free electron laser experiments *Nucl. Instruments Methods Phys. Res. Sect. A Accel. Spectrometers, Detect. Assoc. Equip.* **649** 67–9

[40] Banwell C N and McCash E M 1994 *Fundamentals of Molecular Spectroscopy* (McGraw-Hill)

[41] Bionta M R, Hartmann N, Weaver M, French D, Nicholson D J, Cryan J P, Glownia J M, Baker K, Bostedt C, Chollet M, Ding Y, Fritz D M, Fry A R, Kane D J, Krzywinski J, Lemke H T, Messerschmidt M, Schorb S, Zhu D, White W E and Coffee R N 2014 Spectral encoding method for measuring the relative arrival time between x-ray/optical pulses *Rev. Sci. Instrum.* **85**

[42] Ruddock J M, Zotev N, Stankus B, Bellshaw D, Boutet S, Lane T J, Liang M, Carbajo S, Du W, Minitti M P and Weber P M 2019 Simplicity beneath Complexity: Counting Molecular Electrons Reveals Transients and Kinetics of Photodissociation Reactions *Angew. Chemie - Int. Ed.*

[43] Yong H, Ruddock J M, Stankus B, Ma L, Du W, Goff N, Chang Y, Zotev N, Bellshaw D, Boutet S, Carbajo S, Koglin J E, Liang M, Robinson J S, Kirrander A, Minitti M P and Weber P M 2019 Scattering off molecules far from equilibrium *J. Chem. Phys.* **151** 084301

[44] Carrascosa, A. M., Yong, H., Crittenden, D. L., Weber, P. M. & Kirrander, A. Ab initio calculation of total x-ray scattering from molecules. J. Chem. Theory Comput. 15, 2836–2846 (2019).

[45] Ruddock J M, Yong H, Stankus B, Du W, Goff N, Chang Y, Odate A, Carrascosa A M, Bellshaw D, Zotev N, Liang M, Carbajo S, Koglin J, Robinson J S, Boutet S, Kirrander A, Minitti M P and Weber P M 2019 A deep UV trigger for ground-state ring-opening dynamics of 1,3-cyclohexadiene *Sci. Adv.* **5** 1–8

[46] Schick C P and Weber P M 2001 Ultrafast dynamics in superexcited states of phenol *J. Phys. Chem. A* **105** 3725–34

[47] Cheng W, Evans C L, Kuthirummal N and Weber P M 2001 A 9 eV superexcited state of 1,3-cyclohexadiene revealed by double resonance ionization photoelectron spectroscopy *Chem. Phys. Lett.* **349** 405–10